Bulletin of the Seismological Society of America, Vol. 105, No. 2a, pp. –, April 2015, doi: 10.1785/0120140289

Identifying Active Faults by Improving Earthquake Locations with InSAR Data and Bayesian Estimation: The 2004 Tabuk (Saudi Arabia) Earthquake Sequence

by Wenbin Xu, Rishabh Dutta, and Sigurjón Jónsson

Abstract A sequence of shallow earthquakes of magnitudes ≤5.1 took place in 2004 on the eastern flank of the Red Sea rift, near the city of Tabuk in northwestern Saudi Arabia. The earthquakes could not be well located due to the sparse distribution of seismic stations in the region, making it difficult to associate the activity with one of the many mapped faults in the area and thus to improve the assessment of seismic hazard in the region. We used Interferometric Synthetic Aperture Radar (InSAR) data from the European Space Agency's Envisat and ERS-2 satellites to improve the location and source parameters of the largest event of the sequence (M_w 5.1), which occurred on 22 June 2004. The mainshock caused a small but distinct ~2.7 cm displacement signal in the InSAR data, which reveals where the earthquake took place and shows that seismic reports mislocated it by 3–16 km. With Bayesian estimation, we modeled the InSAR data using a finite-fault model in a homogeneous elastic half-space and found the mainshock activated a normal fault, roughly 70 km southeast of the city of Tabuk. The southwest-dipping fault has a strike that is roughly parallel to the Red Sea rift, and we estimate the centroid depth of the earthquake to be ~3.2 km. Projection of the fault model uncertainties to the surface indicates that one of the west-dipping normal faults located in the area and oriented parallel to the Red Sea is a likely source for the mainshock. The results demonstrate how InSAR can be used to improve locations of moderate-size earthquakes and thus to identify currently active faults.

Introduction

Flanks of active rifts are usually considered to be seismically inactive after the continental extension phase has ended and seafloor spreading has begun (Ebinger, 2005). With its relatively rare intraplate earthquakes, the Arabian shield, which flanks the Red Sea rift, is an example of a seismically inactive flank when compared with the active Red Sea plate boundary. The region is classified as being of relatively low seismic hazard (Giardini *et al.*, 2003), and the Arabian plate is also found to be a geodetically stable region, with no detectable internal strain (ArRajehi *et al.*, 2010). However, several significant earthquakes have occurred on the rift flank in the past two to three decades, including the 1982 M_w 6.2 earthquake in Yemen (Choy and Kind, 1987), the M_w 5.1 Tabuk and M_w 3.7 Badr earthquakes in northwestern Saudi Arabia on 22 June 2004 and 27 August 2009, respectively (Aldamegh *et al.*, 2009, 2012), and the M_L 5.1 event on 23 January 2014 near Jizan in southern Saudi Arabia. Historically, there have also been many damaging earthquakes in the region, both in Saudi Arabia and in Yemen (Ambraseys and Melville, 1983; Ambraseys *et al.*, 1994). For example, the 1941 earthquakes near Jabal Razih in northern Yemen caused 1200 casualties and was felt widely, from Jizan (in southern Saudi Arabia) to the north to Al-Mukalla in southern Yemen (Ambraseys and Melville, 1983). This recent and past activity indicates that some of the numerous mapped faults within the rift flank remain active. However, it is not clear where exactly the historical earthquakes took place, and the source locations of the recent events are not exact enough to associate them with particular mapped faults, due to the sparse regional seismic network. Better identification of the locations of these instrumentally recorded earthquakes are crucial for identifying which faults of the rift flank remain active.

Interferometric Synthetic Aperture Radar (InSAR) has proven to be a useful tool to constrain the location, fault geometry, and slip of many strong ($M_w > 6$) crustal earthquakes (e.g., Weston *et al.*, 2011). InSAR can also be useful to locate smaller earthquakes if they are shallow enough to produce measurable deformation. Lohman and Simons (2005) showed that teleseismic locations of several earthquakes in Iran were off by 10–20 km and that large differences were reported in estimated focal depths. The location

of the 1992 Little Skull Mountain earthquake (M_s 5.4) in Nevada, reported by the Global Centroid Moment Tensor Project, was off by ~42 km from that obtained by InSAR (Lohman *et al.*, 2002). Mellors *et al.* (2004) reported that it is difficult to accurately determine the source parameters of moderate-size earthquakes ($4 < M < 6$) in seismology, especially their epicentral location and focal depth. By systematically comparing earthquake source models derived from InSAR and those from seismic data, Weston *et al.* (2012) found that InSAR provides more accurate location information for shallow events than do seismic catalogs.

The ability of InSAR to locate moderate-size shallow earthquakes to large earthquakes can be exploited to identify active faults. By modeling InSAR data covering the 2008 Reno–Mogul small-magnitude (M_w 5.0) earthquake swarm, Bell *et al.* (2012) suggested the earthquakes were due to strike-slip motion on a previously unknown fault in the Reno basin in Nevada. Similarly, Wicks *et al.* (2013) investigated a series of small earthquakes with InSAR and associated them with a shallow, previously unknown thrust fault beneath the city of Spokane, Washington.

In this study, we use InSAR data to constrain the source location and fault geometry of the 2004 Tabuk earthquake and then use the results to associate the activity to mapped faults on the Red Sea rift flank in northwestern Saudi Arabia. We use Bayesian estimation to generate confidence levels for the estimated model parameters and to propagate the errors to the surface. The results are then compared with the locations of mapped faults.

Geological Setting and the 2004 Tabuk Earthquake

The tectonics of western Arabia are mainly controlled by the geodynamic processes in the Red Sea region (McClusky *et al.*, 2010). The 2004 Tabuk earthquake sequence appears to have occurred on one of the normal faults on the rift flank, ~40 km east of the Red Sea escarpment and within the so-called Hisma plateau of the Arabian shield (Grainger and Hanif, 1989). The Hisma plateau consists of three lithological layers: Precambrian rocks (extending to at least 1 km below sea level) are overlain by Paleozoic sedimentary rocks (sandstone up to 1 km thick) and Cenozoic volcanic rocks of the Harrat ar Raha and Harrat Uwayrid lava fields.

Numerous faults oriented parallel to the axis of the Red Sea rift have been mapped in the Paleozoic sedimentary rocks south and east of Tabuk and north of Harrat Uwayrid (Janjou *et al.*, 1997). Most of these faults are either single normal faults or pairs of faults forming a graben, the majority of which strike between west-northwest and northwest. Many of these faults have a sharp surface expression, without much erosion, and they also appear to have caused offsets to an older regional drainage system with a northeasterly trend (Grainger and Hanif, 1989). In addition, several of the faults on the Hisma Plateau are arcuate with the strike changing from a northwesterly to a northerly trend.

The Tabuk earthquake sequence occurred about 70 km southeast of the city of Tabuk (population >500,000) in June–August 2004 (Fig. 1a). As shown in Figure 2, the sequence started with an M_w 4.4 foreshock on 9 June 2004, followed by several smaller magnitude events ($M_L < 2.5$), before the M_w 5.1 mainshock occurred on 22 June 2004 (the magnitudes are from the International Seismological Centre [ISC]; see Data and Resources). Significant aftershock activity continued until 29 August 2004, with a total of 380 earthquakes recorded (Aldamegh *et al.*, 2009). Although the earthquake sequence caused only minor damage, the mainshock was widely felt in northwestern Saudi Arabia (Aldamegh *et al.*, 2009).

Different moment magnitudes and locations are reported for the M_w 5.1 mainshock, now referred to as the Tabuk earthquake in various seismic studies and catalogs (Fig. 1b). Using regional waveform inversion, Aldamegh *et al.* (2009) reported a normal-faulting mechanism with an M_w 5.1, a 4 km focal depth, and a location that is ~4 km further west than in the National Earthquake Information Center (NEIC) and the ISC catalogs. The strike is more southerly and the dip is shallower for the mainshock in the Zürich Moment Tensors (ZUR_RMT) catalog than those given in the other reports, whereas the Mediterranean Network Regional Centroid Moment Tensors (MED_RCMT) catalog has the main event located about 17 km further to the north. In summary, the distances between the epicentral locations in the above reports is 2–19 km and the depths vary from 4 to 15 km, making it impossible to associate the earthquake with one of the many mapped faults in the area (Fig. 1b).

InSAR Observations

To determine the exact location of the Tabuk earthquake, we studied the ground deformation associated with the earthquake sequence using ascending and descending C-band (5.6 cm wavelength) InSAR data from the European Space Agency's ERS-2 and Envisat satellites (Table 1). We processed the data with the GAMMA software (see Data and Resources) and used the Shuttle Radar Topography Mission digital elevation model (Farr *et al.*, 2007) to simulate and eliminate the topographic signals. The interferogram noise was first reduced by multilooking to about 40 m pixel spacing and then by filtering (Goldstein and Werner, 1998). The interferograms were then unwrapped using the minimum cost flow method (Chen and Zebker, 2000), then geocoded into the 1984 World Geodetic System (WGS84) coordinate system.

Unwanted atmospheric signals are one of the most limiting factors in applications of repeat-pass InSAR (Zebker *et al.*, 1997; Li *et al.*, 2012). To reduce these effects, we estimated and removed linearly elevation-dependent atmospheric signals in the region near the epicenter (Xu *et al.*, 2011). We then stacked all available interferograms from within the same frame to improve the signal-to-noise ratio. The resulting deformation pattern is very similar in both the ascending and descending interferograms, indicating that the

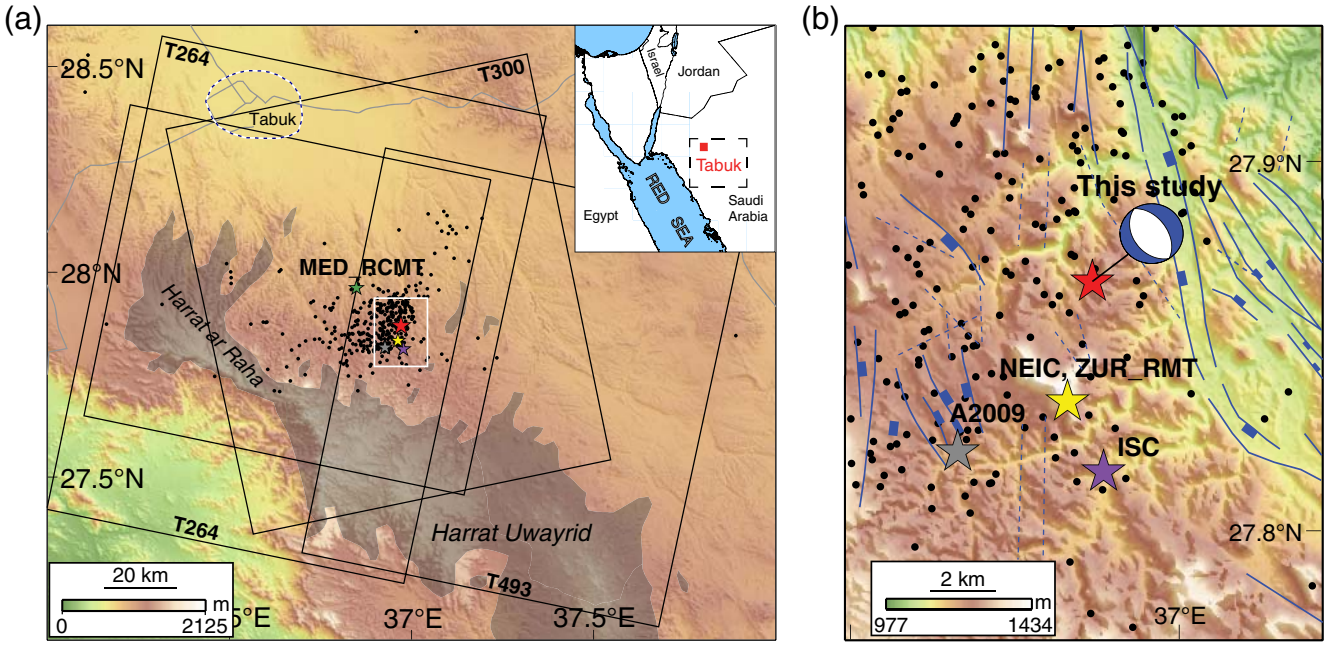

Figure 1. Location of the 2004 Tabuk earthquake sequence in northwestern Saudi Arabia. (a) Black dots show earthquake locations from the International Seismological Centre (ISC) catalog in 2004, and stars indicate mainshock locations from the different seismic catalogs in comparison to our study. The coverage of the Harrat ar Raha and Harrat Uwayrid lava fields is shown in dark gray. Black boxes outline ascending- and descending-orbit Synthetic Aperture Radar frames, respectively. The inset shows the location of the study area. (b) Enlarged view of the epicentral area (white rectangle in [a]) with mapped faults (Grainger and Hanif, 1989). Sources of locations are as follows: A2009, Aldamegh *et al.*, 2009, location; MED_RCMT, Mediterranean Network Regional Centroid Moment Tensors; NEIC, National Earthquake Information Center; and ZUR_RMT, Zürich Moment Tensors. The color version of this figure is available only in the electronic edition.

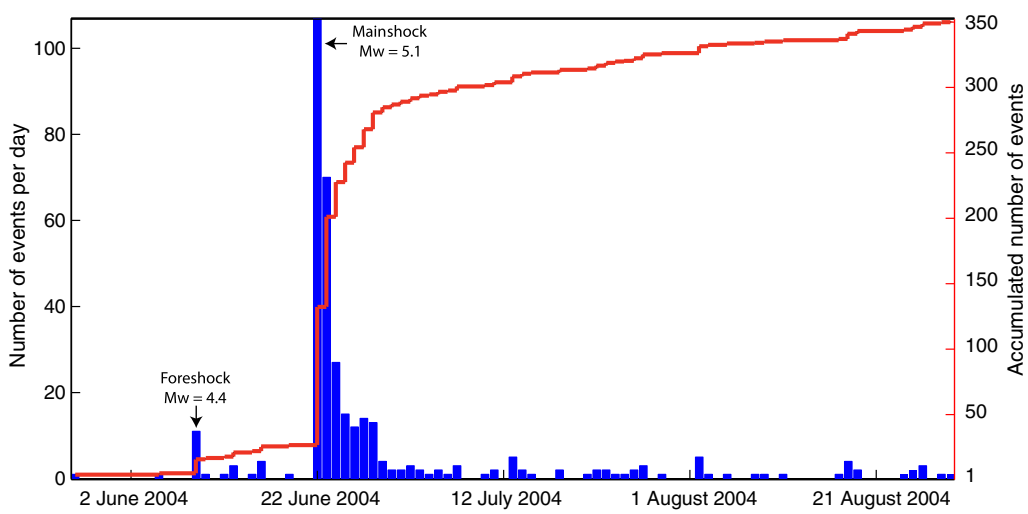

Figure 2. Number of events per day and cumulative number of events versus time of 2004 Tabuk earthquake sequence (data from the ISC catalog). The color version of this figure is available only in the electronic edition.

dominant coseismic displacement is vertical (Fig. 3a–d). The maximum line-of-sight (LOS) displacement is ~2.7 cm at the center of an ~40 km^2 elliptical deforming area.

The measured LOS displacement $\mathbf{d}_{\mathrm{LOS}}$ is a projection of the 3D surface displacement field onto the unit look vector from the ground to the satellite:

$$d_{\mathrm{LOS}} = [U_{\mathrm{n}} \sin\varphi - U_{\mathrm{e}} \cos\varphi] \sin\lambda + U_{\mathrm{u}} \cos\lambda + \epsilon_{\mathrm{LOS}} \quad (1)$$

(Fialko *et al.*, 2001), in which U_{n}, U_{e}, and U_{u} are the north, east, and up ground displacement, respectively; φ is the satellite flight direction (clockwise from north); λ is the radar incidence angle; and ϵ_{LOS} is the measurement error. With

Table 1
Information about the Interferometric Synthetic Aperture Radar (InSAR) Data used in This Study

Satellite	Flight Direction	Track Number	Date (yyyy/mm/dd)	Orbit	Perpendicular Baseline (m)
Envisat	Descending	264	2004/01/17	9837	0
			2006/02/25	20859	−119
			2006/12/02	24867	123
			2008/05/10	32382	223
ERS-2	Ascending	300	2003/07/28	43240	0
			2005/06/27	53260	−163
	Descending	264	2004/01/17	45709	0
			2004/08/14	48715	171
			2005/02/05	51220	145
		493	2003/09/15	43934	0
			2005/02/21	51449	56

three similar descending LOS observations and one ascending observation, we decomposed the four interferograms into two orthogonal displacement directions (east–west and vertical), assuming the deformation in the north direction is negligible (Wright *et al.*, 2004). Wicks *et al.* (2013) showed that ignoring the northward deformation usually brings only small errors to the vertical and east–west component of the deformation field of small magnitude earthquakes.

To solve for the 2D displacement field, we used a weighted least-squares method with the weight inversely proportional to the variance of each dataset. The derived east and vertical ground displacement maps show the main component of coseismic displacement is subsidence of up to ~2.9 cm (Fig. 4), consistent with what would be expected from a normal-faulting earthquake. The derived east displacements are smaller and do not exhibit as clear a pattern as the vertical displacements, probably due to residual atmospheric effects.

Modeling of the Observed Deformation

In the modeling, we used a single rectangular dislocation (Okada, 1985) with uniform slip to model the interferograms, assuming a homogeneous and isotropic elastic half-space (Poisson's ratio $\nu = 0.25$, shear modulus $\mu = 25$ GPa). We subsampled our data points using the quadtree method (Jónsson *et al.*, 2002) (Fig. 3e–h), treated the observations as independent in the optimization, and weighted them according to their variances.

The observed ground deformation $\mathbf{d}$ can be expressed as a function g of the model parameters $\mathbf{m}$:

$$\mathbf{d} = g(\mathbf{m}) + \varepsilon, \tag{2}$$

in which g is a function that relates the ground displacements to the model parameters; $\mathbf{m}$ defines the location, strike, dip, depth, dimensions (length and width) and slip of the fault plane; and ε are observational errors. We fix the strike slip to be 0, as suggested by the focal mechanism (Aldamegh *et al.*, 2009), then allow the nonlinear optimization to search for any fault dip (0°–90°) and for any possible fault strike.

We seek the model parameters that minimize the weighted root mean square misfit function between $\mathbf{d}$ and $g(\mathbf{m})$:

$$\Phi = ||\mathbf{W}[\mathbf{d} - g(\mathbf{m})]||_2, \tag{3}$$

in which $\mathbf{W}$ is the weight matrix based on the estimated observation errors. We find the optimal fault model parameters by minimizing equation (3) using nonlinear optimization, first by using a Monte Carlo-type simulated annealing algorithm (Cervelli *et al.*, 2001), followed by a gradient-based method. Our optimal model fault is southwesterly dipping with a N326.5°W strike (i.e., is parallel to the Red Sea), is 3.5 km long, extending from 2.7 to 3.7 km depth, and has 29 cm of normal slip (Table 2). The predicted ground displacements fit the observations well (Fig. 3). The optimal model parameters together with several solutions derived from seismic data (i.e., NEIC, ISC, ZUR_RMT, and MED_RCMT) can be found in Table 2.

Bayesian Uncertainty Estimation

The optimal fault parameter solution presented in the section above does not provide information about how well the model parameters are constrained by the observations. To quantify the model parameter uncertainties, we use Bayesian estimation to determine the posterior probability distribution of the model parameters given the available data.

Considering an $\mathbf{M}$-dimensional model parameter space and $\mathbf{D}$-dimensional data space, we define the posterior probability density function (PDF) $\sigma_{\mathbf{M}}(\mathbf{m}|\mathbf{d})$ as given by Tarantola (2005):

$$\sigma_{\mathbf{M}}(\mathbf{m}|\mathbf{d}) = k\rho_{\mathbf{M}}(\mathbf{m})\mathbb{L}(\mathbf{m}|\mathbf{d}), \tag{4}$$

in which k is a normalizing constant and $\rho_{\mathbf{M}}(\mathbf{m})$ is the prior probability distribution of the model parameters. We used the size of the Tabuk earthquake of M_w 5.1 (Aldamegh *et al.*, 2009) as *a priori* knowledge.

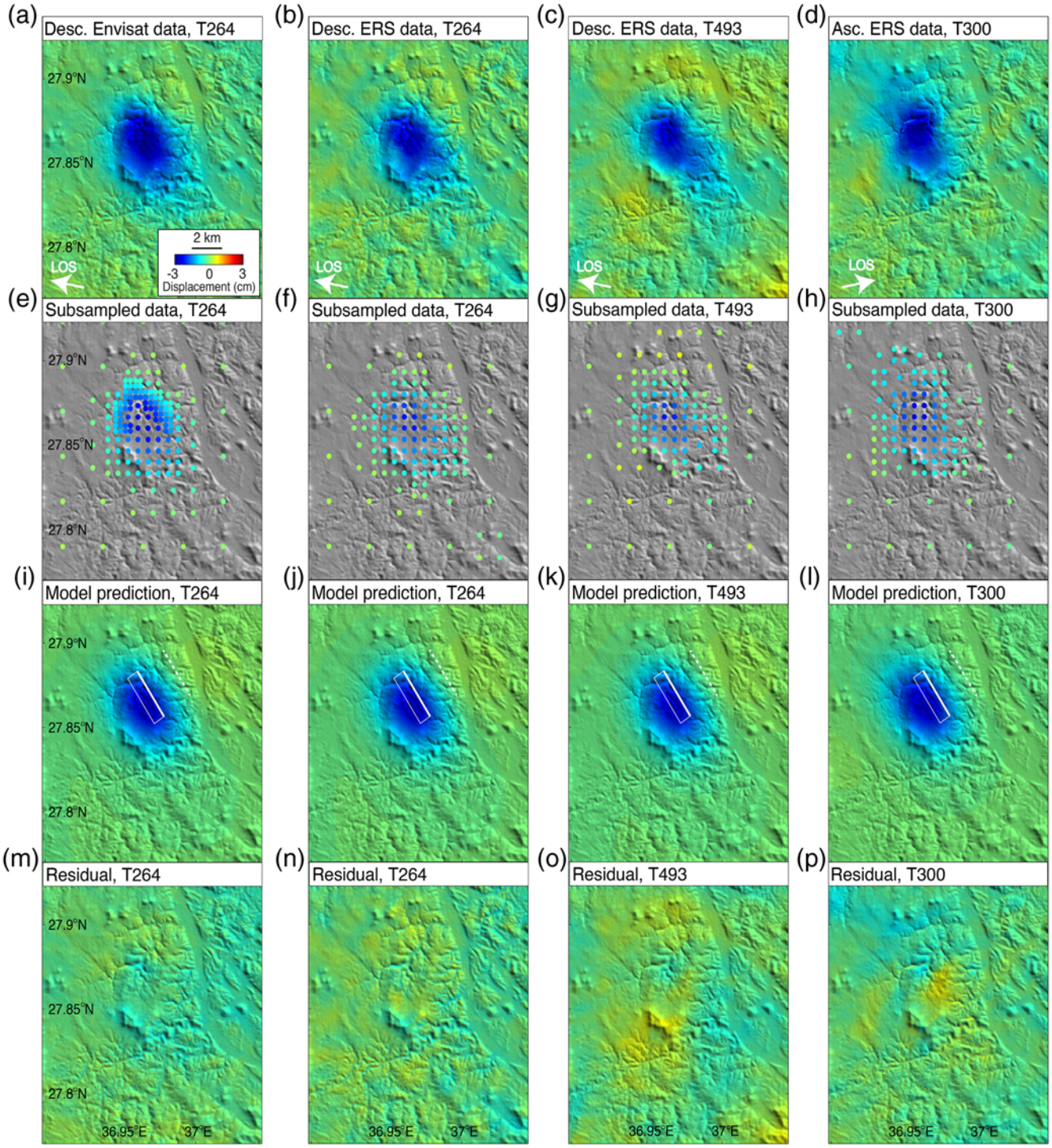

Figure 3. Coseismic Interferometric Synthetic Aperture Radar (InSAR) data of the Tabuk earthquake in comparison with the optimal model prediction. (a–d) The four unwrapped interferograms used in this study, with negative line-of-sight displacement values indicating movement away from the satellites (primarily subsidence). The scale is the same for all panels. (e–h) Quadtree subsampled InSAR data. (i–l) Predicted InSAR data from the optimal model (Table 2) with the surface projection of the estimated fault plane indicated by a white rectangle (upper edge in bold) and extrapolation of the fault plane to the surface shown by a white dashed line. (m–p) The residuals between the (a–d) observed and (i–l) predicted interferograms. The color version of this figure is available only in the electronic edition.

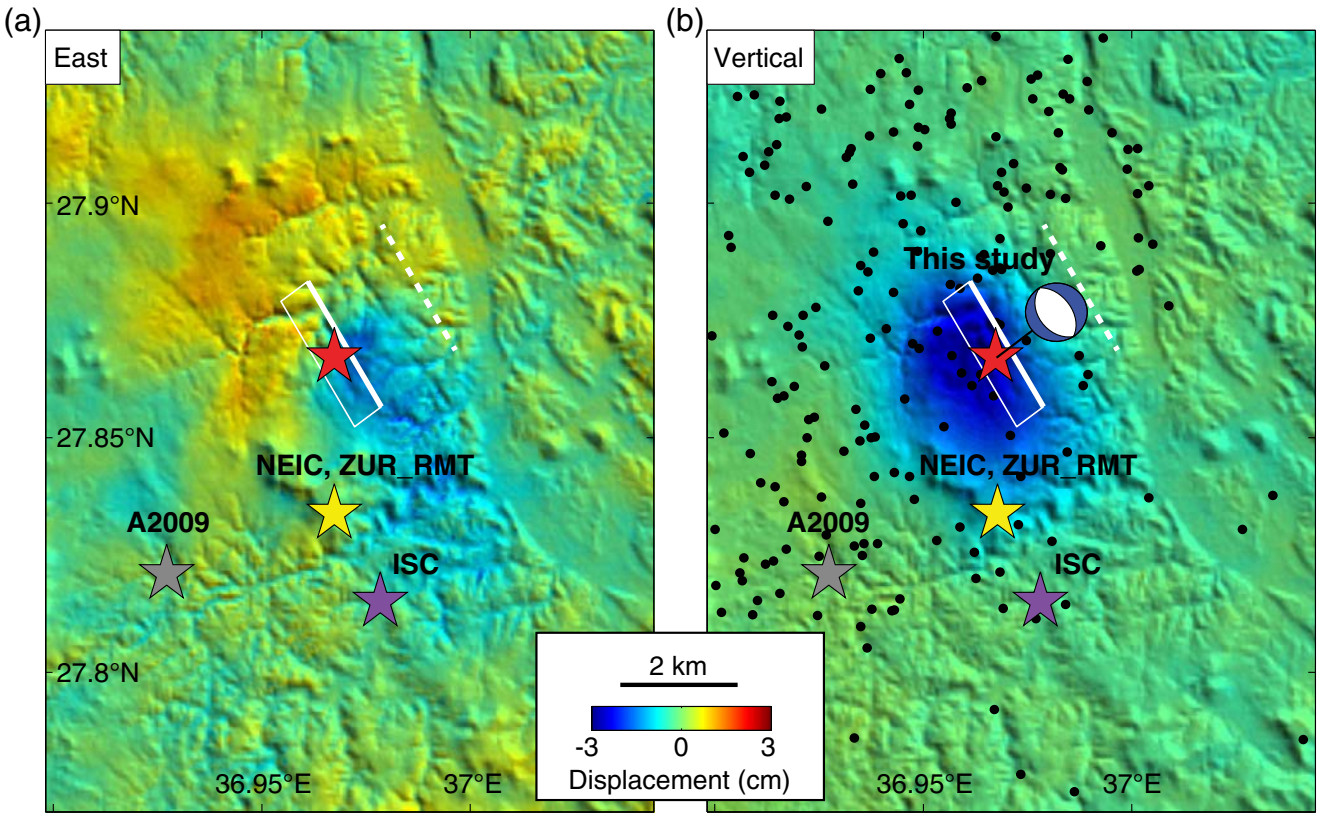

Figure 4. (a) East and (b) vertical ground displacement components derived from the interferograms shown in Figure 3a–d. Positive values indicate movement to the east and up. Seismicity and sources of information are as in Figure 1b. The color version of this figure is available only in the electronic edition.

$$\rho_{\mathbf{M}}(\mathbf{m}) = \frac{1}{\sqrt{(2\pi\alpha^2)}} \exp\left\{-\frac{1}{2\alpha^2}[M(\mathbf{m}) - 5.1]^2\right\}, \quad (5)$$

in which $M(\mathbf{m})$ is the moment magnitude and α is chosen to be 0.01. We assume the prior distribution to be a Gaussian distribution centered at 5.1 with a small standard deviation. $\mathbb{L}(\mathbf{m}|\mathbf{d})$ is the likelihood function expressing how the data explain the model parameters:

$$\mathbb{L}(\mathbf{m}|\mathbf{d}) = \int_{\mathbf{D}} \rho_{\mathbf{D}}(\mathbf{d})\Theta(\mathbf{d}|\mathbf{m})d\mathbf{d}, \quad (6)$$

in which $\Theta(\mathbf{d}|\mathbf{m})$ is the conditional probability distribution representing the correlation between $\mathbf{d}$ and $\mathbf{m}$ and is defined as a Dirac-delta function, $\delta[\mathbf{d} - g(\mathbf{m})]$, assuming the data match perfectly to the model parameters. $\rho_{\mathbf{D}}(\mathbf{d})$ is the prior PDF over the data, expressed here with a Gaussian PDF:

$$\rho_{\mathbf{D}}(\mathbf{d}) = \frac{1}{\sqrt{(2\pi)^n|\Sigma|}} \exp\left\{-\frac{1}{2}[\mathbf{d} - g(\mathbf{m})]^T\Sigma^{-1}[\mathbf{d} - g(\mathbf{m})]\right\}, \quad (7)$$

Table 2
Estimated Fault Parameters for the June 2004 Tabuk Earthquake

Reference*	Latitude (°)	Longitude (°)	Length (km)	Width (km)	Depth (km)	Strike (°)	Dip (°)	Dip Slip (cm)	M_w
NEIC	27.835	36.966	–	–	10†	–	–	–	3.7 (M_w)
ISC	27.816	36.977	–	–	10†	–	–	–	5.1
ZUR_RMT	27.835	36.966	–	–	12†	129, 300	19, 71	–	5.1
MED_RCMT	27.96	36.85	–	–	15†	136, 320	30, 60	–	5.1
Aldamegh *et al.* (2009)	27.822	36.926	–	–	4	137, 329	40, 50	–	5.1
This study‡	$27.866^{+1.0\text{ km}}_{-0.9\text{ km}}$	$36.969^{+0.6\text{ km}}_{-1.4\text{ km}}$	$3.5^{+2.2}_{-2.6}$	$1.3^{+4.0}_{-0.6}$	$3.2^{+0.7}_{-1.2}$	$146.5^{+23.5}_{-26.1}$, $326.5^{+32.6}_{-40.6}$	50^{+26}_{-13}	29^{+20}_{-22}	$5.0^{+0.7}_{-1.0}$

*NEIC, National Earthquake Information Center; ISC, International Seismological Centre; ZUR_RMT, Zurich Moment Tensors; MED_RCMT, Mediterranean Network Regional Centroid Moment Tensors.

†Fixed parameter.

‡Longitude and latitude are for the center of the fault plane at the upper edge, the depth is the centroid location. The uncertainties are 95% confidence intervals of the model parameters.

in which Σ is the data covariance matrix. Using the equations above, we thus define the posterior density as given by Tarantola (2005):

$$\sigma_{\mathbf{M}}(\mathbf{m}|\mathbf{d}) = \mathrm{k}\exp\left\{-\frac{1}{2}[\mathbf{d} - g(\mathbf{m})]^T\Sigma^{-1}[\mathbf{d} - g(\mathbf{m})] - \frac{1}{2\alpha^2}[M(\mathbf{m}) - 5.1]^2\right\}. \quad (8)$$

We implemented one of the Markov chain Monte Carlo methods, called the Metropolis–Hastings algorithm (Hastings, 1970), to evaluate this high-dimensional posterior probability distribution. The algorithm draws samples from a simple proposed distribution centered at the present search location, rather than from the posterior distribution directly. It rejects or accepts the following set of model parameters based on a condition that more likely models are always accepted and less likely models are only accepted according to a certain acceptance ratio. We use a multivariate Gaussian distribution as the proposed distribution with a standard deviation, that is, a tenth of the difference between the lower and the upper search limits of the respective model parameters. The obtained population of models was treated for autocorrelation by thinning using the Geyer iterated monotone sequence estimator heuristic (Geyer, 1992). The remaining thinned model population was thus considered representative of the posterior PDF.

The resulting marginal distributions of the model parameters from the Bayesian estimation show the location and strike of the fault are better constrained than the fault geometry and slip (Fig. 5). The optimal location of the fault correlates well with the peak of the Bayesian estimation. For the fault length, width, depth, and dip, we find relatively broad marginal distribution peaks and some degree of asymmetry. The marginal distribution for the fault strike indicates the source fault most likely dips to the southwest, although we cannot exclude the possibility of a northeasterly dipping fault (Fig. 5g).

The 95% confidence intervals for all the parameters are listed in Table 2. None of the epicentral locations reported in the seismic catalogs fall within the 95% confidence intervals as estimated by InSAR (Table 2). However, the strike and dip of the fault estimated from seismic catalogs are well within the InSAR 95% confidence intervals, as these parameters are probably better determined from seismic data in this case.

Discussion and Conclusions

The InSAR analysis and inverse modeling presented here show the 2.7 cm LOS displacement observed due to the 22 June 2004 M_w 5.1 Tabuk earthquake was caused by ~29 cm of fault slip on a normal-fault oriented parallel to the Red Sea. Although the fault strike and dip are not particularly well constrained by the InSAR data, the results indicate the minimum regional compressional stress σ_3 has a direction that is roughly perpendicular to the Red Sea. This is similar to that suggested for other significant normal-faulting earthquakes on the northwestern Saudi Arabian rift flank (Pallister *et al.*, 2010; Aldamegh *et al.*, 2012). The 2009 Badr earthquake occurred 450 km southeast of the Tabuk earthquake and about 50 km away from the Red Sea escarpment; it was also a normal-faulting event with a similar strike parallel to the Red Sea (Aldamegh *et al.*, 2012). Also in 2009, a rifting event took place in Harrat Lunayyir, about 300 km south-southeast of the Tabuk earthquake and well within the rift flank. Modeling of the observed deformation indicated that a magmatic dike intruded with an orientation that was roughly parallel to the Red Sea (Pallister *et al.*, 2010). The activity was also associated with a major seismic sequence, of which the largest earthquake (M_w 5.7) exhibited a normal slip on a northeasterly dipping fault. All these events show the Red Sea tensional stress field currently extends at least several tens of kilometers into the rift flank.

By extrapolating the estimated buried fault plane of the Tabuk earthquake to the surface, we are able to determine whether or not the earthquake was associated with a mapped fault (Fig. 6). The extension of the best-fitting fault plane intersects the surface just west of a mapped graben, which has a similar orientation as the estimated fault (Fig. 6). However, the width of the graben is only 1–2 km, indicating the graben-bounding faults do not extend far into the crust. The source fault could be a southeast extension of one of the mapped lineations in the area or related to a lineation that runs to the west of and is parallel to where the best-fitting fault plane hits the surface (solid and dashed lines in Fig. 6). In addition, the possibility that the source fault is northeasterly dipping cannot be excluded (Fig. 5g), and extensions of this class of solutions to the surface appears to match with two northeasterly dipping faults to the southwest of the epicenter, although both appear to bound narrow grabens (Fig. 6b). To better assess the hazard posed by the faults in this area and the associated risks to human populations, additional geological and geophysical studies should be carried out to determine which of the mapped faults may still be active. In particular, an installation of a local seismic network would provide microearthquake locations in the area and should help in associating them with certain faults. Also, as seismic data can well constrain the mechanism of moderately sized earthquakes and as InSAR data can efficiently locate shallow events (Lohman *et al.*, 2002), the model parameters of the Tabuk earthquake should be better constrained when the data are used together. Future work should therefore consider a joint inversion of seismic and geodetic data to better resolve the ambiguity of strike and dip of the earthquake-generating fault.

Despite the ambiguity in associating the Tabuk earthquake with a particular mapped fault, the results still demonstrate that InSAR is able to more precisely determine the location and depth of shallow, moderate-size earthquakes. All seismic solutions mislocated the earthquake by 3–16 km and overestimated its depth. The seismic solutions also do not agree with each other on the mainshock's location, and none of them falls within the area of observed deformation

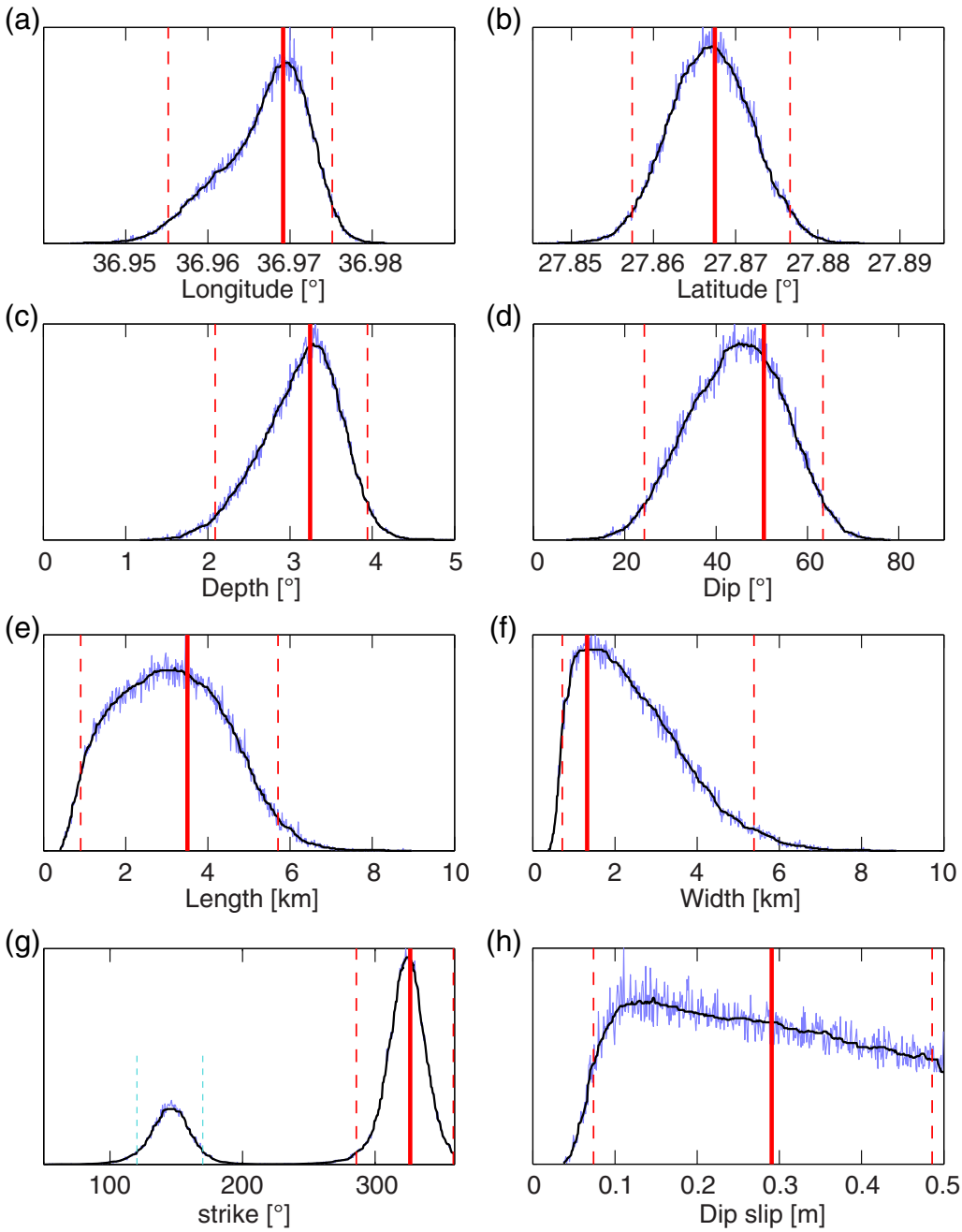

Figure 5. Posterior marginal probability distributions for the parameters of the Tabuk earthquake fault model. The black lines show median-filtered probability distribution values. The thick solid lines indicate the best-fit model parameters, and dashed lines correspond to 95% confidence intervals; the shorter set of dashed lines in (g) bracket a second set of possible, yet less likely, strike values. The color version of this figure is available only in the electronic edition.

(Fig. 4a–d). Similar to our study, Wang *et al.* (2014) found that InSAR has an advantage over body-wave seismology in determining earthquake locations and depths by looking at four normal earthquakes outside the center of the Pumqu–Xainza rift in Tibet. Furthermore, Elliott *et al.* (2010) and Wang *et al.* (2014) reported, despite the strength of InSAR in locating earthquakes, that it can still be difficult to associate located events with known tectonic structures in geologically complex regions.

Shallow earthquakes of moderate size can be devastating (Barnhart *et al.*, 2011). For example, the M_w 6.2 Christchurch, New Zealand, earthquake, which took place in an area that was not considered particularly active, damaged more than 100,000 buildings and caused over 180 casualities (Kalkan, 2011). Rapid urbanization and population growth in and around Tabuk have led to increased risk and vulnerability to earthquakes. More data are becoming available with the expansion of seismic networks on the Arabian Peninsula and

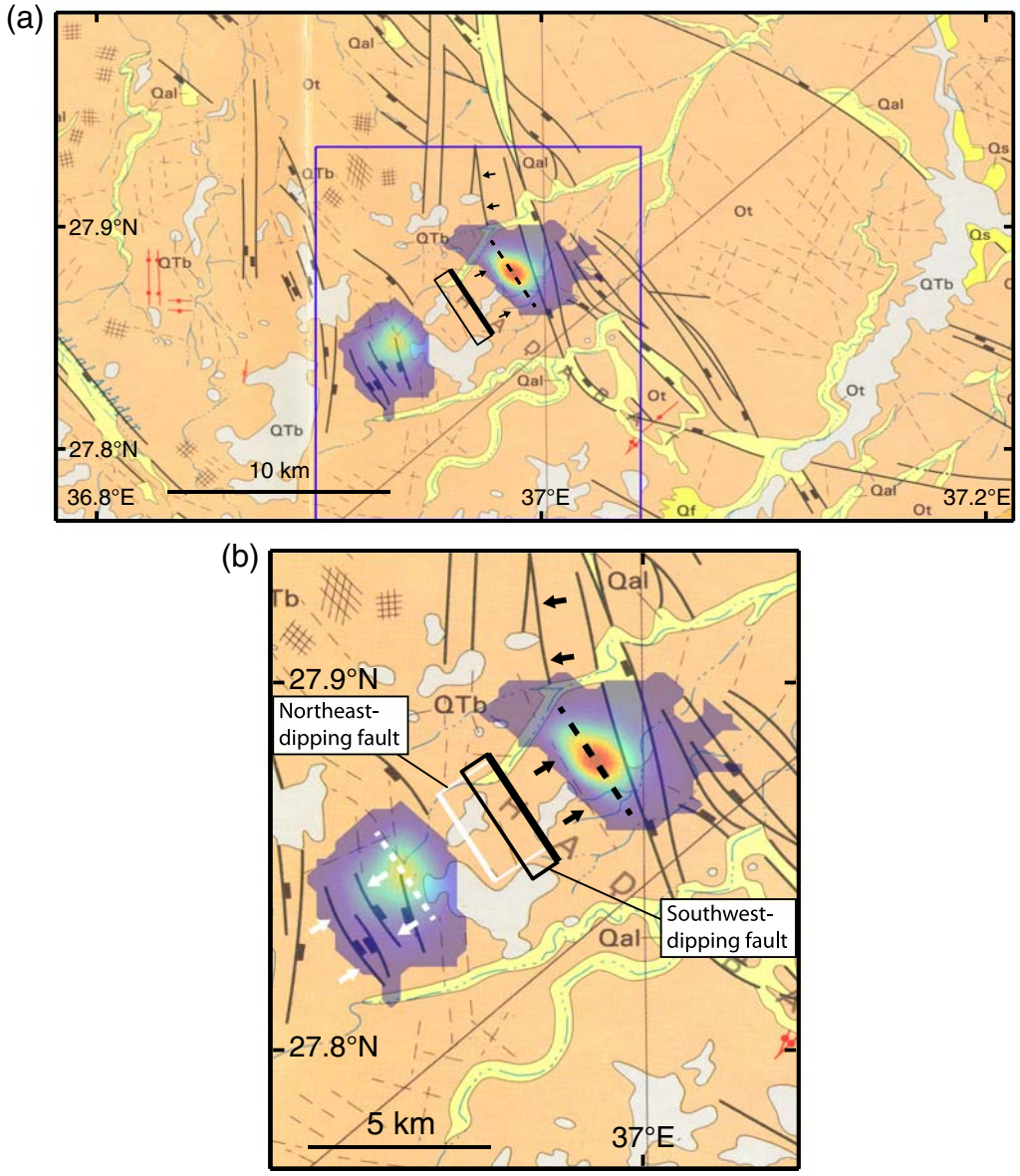

Figure 6. The fault-model results on a geological map of the study area (from Grainger and Hanif, 1989). (a) The rectangle shows the coverage of Figures 1b, 3, and 4, and the black dashed line indicates the surface extrapolation of the optimum Tabuk fault model. The transparent areas show the probability density of surface extrapolations of southwest-dipping (more likely) and northeast-dipping (less likely) faults. Solid and dashed black lines indicate mapped and inferred faults, respectively, with the arrows pointing out the possible source faults. Ot, Tabuk formation; Qal, alluvium; Qf, alluvial fan deposits; and QTb, basalt. (b) Enlarged view of the study area (rectangle in [a]). The less-likely northeast-dipping fault is shown in white. The color version of this figure is available only in the electronic edition.

with new InSAR satellite missions (e.g., Sentinel-1 and Advanced Land Observing Satellite-2). All of which will improve our knowledge of seismically active faults in the region and thus lead to better seismic-hazard estimates.

Data and Resources

The International Seismological Centre (ISC) bulletin event catalog was searched using http://www.isc.ac.uk/iscbulletin/search/catalogue/ (last accessed October 2013). Earthquake locations used in this article came from Aldamegh *et al.* (2009), listed in the references. Figure 1 was made using the Generic Mapping Tools version 4.5.9 (www.soest.hawaii.edu/gmt, last accessed August 2014; Wessel and Smith, 1998). The GAMMA Synthetic Aperture Radar (SAR) and Interferometry Software is a commercial software that allows processing of SAR data for airborne and spaceborne SAR systems (http://www.gamma-rs.ch/gamma.html; last accessed June 2013).

Acknowledgments

The authors would like to thank Ahmet Akoglu (King Abdullah University of Science and Technology [KAUST]) for reviewing an early version

of the manuscript. Comments made by Associate Editor Roland Bürgmann and two anonymous reviewers helped improve the manuscript. The Synthetic Aperture Radar images were provided by the European Space Agency through the Category-1 project #6703. The research reported in this publication was supported by KAUST.

References

Aldamegh, K. S., K. A. Elenean, H. M. Hussein, and A. J. Rodgers (2009). Source mechanisms of the June 2004 Tabuk earthquake sequence, eastern Red Sea margin, Kingdom of Saudi Arabia, *J. Seismol.* **13,** 561–576.

Aldamegh, K. S., H. H. Moussa, S. N. Al-Arifi, S. S. R. Moustafa, and M. H. Moustafa (2012). Focal mechanism of Badr earthquake, Saudi Arabia, of August 27, 2009, *Arab. J. Geosci.* **5,** 599–606.

Ambraseys, N. N., and C. P. Melville (1983). Seismicity of Yemen, *Nature* **303,** 321–323.

Ambraseys, N. N., C. P. Melville, and R. D. Adams (1994). *The Seismicity of Egypt, Arabia and the Red Sea: A Historical Review*, Cambridge University Press, Cambridge.

ArRajehi, A., S. McClusky, R. Reilinger, M. Daoud, A. Alchalbi, S. Ergintav, F. Gomez, J. Sholan, F. Bou-Rabee, G. Ogubazghi, B. Haileab, S. Fisseha, L. Asfaw, S. Mahmoud, A. Rayan, R. Bendik, and L. Kogan (2010). Geodetic constraints on present-day motion of the Arabian plate: Implications for Red Sea and Gulf of Aden rifting, *Tectonics* **29,** TC3011, doi: 10.1029/2009TC002482.

Barnhart, W. D., M. J. Willis, R. B. Lohman, and A. K. Melkonian (2011). InSAR and optical constraints on fault slip during the 2010–2011 New Zealand earthquake sequence, *Seismol. Res. Lett.* **82,** 815–823.

Bell, J. W., F. Amelung, and C. D. Henry (2012). InSAR analysis of the 2008 Reno-Mogul earthquake swarm: Evidence for westward migration of Walker Lane style dextral faulting, *Geophys. Res. Lett.* **39,** L18306, doi: 10.1029/2012GL052795.

Cervelli, P., M. H. Murray, P. Segall, Y. Aoki, and T. Kato (2001). Estimating source parameters from deformation data, with an application to the March 1997 earthquake swarm off the Izu Peninsula, Japan, *J. Geophys. Res.* **106,** 11,217–11,237.

Chen, C. W., and H. A. Zebker (2000). Network approaches to two-dimensional phase unwrapping: Intractability and two new algorithms, *J. Opt. Soc. Am.* **17,** 401–414.

Choy, G. L., and R. Kind (1987). Rupture complexity of a moderate-sized (m_b 6.0) earthquake: Broadband body-wave analysis of the North Yemen earthquake of 13 December, 1982, *Bull. Seismol. Soc. Am.* **77,** 28–46.

Ebinger, C. (2005). Continental breakup: The East African perspective, *Astron. Geophys.* **46,** 2.16–2.21.

Elliott, J. R., R. J. Walters, P. C. England, J. A. Jackson, Z. Li, and B. Parsons (2010). Extension on the Tibetan plateau: Recent normal faulting measured by InSAR and body wave seismology, *Geophys. J. Int.* **183,** 503–535.

Farr, T. G., P. A. Rosen, E. Caro, R. Crippen, R. Duren, S. Hensley, M. Kobrick, M. Paller, E. Rodriguez, L. Roth, D. Seal, S. Shaffer, J. Shimada, J. Umland, M. Werner, M. Oskin, D. Burbank, and D. Alsdorf (2007). The Shuttle Radar Topography Mission, *Rev. Geophys.* **45,** RG2004, doi: 10.1029/2005RG000183.

Fialko, Y., M. Simons, and D. Agnew (2001). The complete (3-D) surface displacement field in the epicentral area of the 1999 M_w 7.1 Hector Mine earthquake, California, from space geodetic observations, *Geophys. Res. Lett.* **28,** 3063–3066.

Geyer, C. J. (1992). Practical Markov chain Monte Carlo, *Stat. Sci.* **7,** 473–511.

Giardini, D., G. Grünthal, K. M. Shedlock, and P. Zhang (2003). The GSHAP global seismic hazard map, in *International Handbook of Earthquake & Engineering Seismology*, W. Lee, H. Kanamori, P. Jennings, and C. Kisslinger (Editors), International Geophysics Series 81 B, Academic Press, Amsterdam, The Netherlands, 1233–1239.

Goldstein, R. M., and C. L. Werner (1998). Radar interferogram filtering for geophysical applications, *Geophys. Res. Lett.* **25,** 4035–4038.

Grainger, D. J., and M. R. Hanif (1989). Geologic map of the Shaghab quadrangle, Kindom of Saudi Arabia, *Geoscience Map GM-109C*, scale 1:250,000, sheet 27B, Directorate General of Mineral Resources, Ministry of Petroleum and Mineral Resources, Kingdom of Saudi Arabia, 31 pp.

Hastings, W. K. (1970). Monte Carlo sampling methods using Markov chains and their applications, *Biometrika* **57,** 97–109.

Janjou, D., M. A. Halawani, J. M. Brosse, M. S. Al-Muallem, J. F. Becq-Giraudon, J. Dagain, A. Genna, P. Razin, M. J. Roobol, H. Shorbaji, and R. Wyns (1997). Explanatory notes to the geologic map of the Tabuk Quadrangle, Kingdom of Saudi Arabia, *Geoscience Map GM-137*, scale 1:250,000, sheet 28B, Deputy Ministry for Mineral Resources, Ministry of Petroleum and Mineral Resources, Kingdom of Saudi Arabia, 49 pp.

Jónsson, S., H. Zebker, P. Segall, and F. Amelung (2002). Fault slip distribution of the 1999 M_w 7.1 Hector Mine, California, earthquake, estimated from satellite radar and GPS measurements, *Bull. Seismol. Soc. Am.* **92,** 1377–1389.

Kalkan, E. (2011). Preface to the focused issue on the 22 February 2011 magnitude 6.2 Christchurch earthquake, *Seismol. Res. Lett.* **82,** 765–766.

Li, Z. W., W. B. Xu, G. C. Feng, J. Hu, C. C. Wang, X. L. Ding, and J. J. Zhu (2012). Correcting atmospheric effects on InSAR with MERIS water vapour data and elevation-dependent interpolation model, *Geophys. J. Int.* **189,** 898–910.

Lohman, R. B., and M. Simons (2005). Locations of selected small earthquakes in the Zagros mountains, *Geochem. Geophys. Geosys.* **6,** Q03001, doi: 10.1029/2004GC000849.

Lohman, R. B., M. Simons, and B. Savage (2002). Location and mechanism of the Little Skull Mountain earthquake as constrained by satellite radar interferometry and seismic waveform modeling, *J. Geophys. Res.* **107,** no. B6, doi: 10.1029/2001JB000627.

McClusky, S., R. Reilinger, G. Ogubazghi, A. Amleson, B. Healeb, P. Vernant, J. Sholan, S. Fisseha, L. Asfaw, R. Bendick, and L. Kogan (2010). Kinematics of the southern Red Sea-Afar Triple Junction and implications for plate dynamics, *Geophys. Res. Lett.* **37,** L05301, doi: 10.1029/2009GL041127.

Mellors, R. J., H. Magistrale, P. Earle, and A. Cogbill (2004). Comparison of four moderate-size earthquakes in southern California using seismology and InSAR, *Bull. Seismol. Soc. Am.* **94,** 2004–2014.

Okada, Y. (1985). Surface deformation due to shear and tensile faults in a half-space, *Bull. Seismol. Soc. Am.* **75,** 1135–1154.

Pallister, J. S., W. A. McCausland, S. Jónsson, Z. Lu, H. M. Zahran, S. Hadidy, A. Aburukbah, I. C. F. Stewart, P. R. Lundgren, R. A. White, and M. R. H. Moufti (2010). Broad accommodation of rift-related extension recorded by dyke intrusion in Saudi Arabia, *Nature Geosci.* **3,** 705–712.

Tarantola, A. (2005). *Inverse Problem Theory and Methods for Model Parameter Estimation*, Society for Industrial and Applied Mathematics, Philadelphia, Pennsylvania.

Wang, H., J. R. Elliott, T. J. Craig, T. J. Wright, and J. Liu-Zeng (2014). Normal faulting sequence in the Pumqu-Xainza Rift 1 constrained by InSAR and teleseismic body-wave seismology, *Geochem. Geophys. Geosys.* **15,** 2947–2963.

Wessel, P., and W. H. F. Smith (1998). New improved version of the Generic Mapping Tools released, *Eos Trans. AGU* **79,** 579–579.

Weston, J., A. M. G. Ferreira, and G. J. Funning (2011). Global compilation of interferometric synthetic aperture radar earthquake source models: 1. Comparisons with seismic catalogs, *J. Geophys. Res.* **116,** no. B08408, doi: 10.1029/2010JB008131.

Weston, J., A. M. G. Ferreira, and G. J. Funning (2012). Systematic comparisons of earthquake source models determined using InSAR and seismic data, *Tectonophysics* **532,** 61–81.

Wicks, C., C. Weaver, P. Bodin, and B. Sherrod (2013). InSAR Evidence for an active shallow thrust fault beneath the city of Spokane Washington, USA, *J. Geophys. Res.* **118,** 1268–1276.

Wright, T. J., B. E. Parsons, and Z. Lu (2004). Toward mapping surface deformation in three dimensions using InSAR, *Geophys. Res. Lett.* **31,** L01607, doi: 10.1029/2003GL018827.

Xu, W., Z. Li, X. Ding, and J. Zhu (2011). Interpolating atmospheric water vapor delay by incorporating terrain elevation information, *J. Geodesy.* **85,** 555–564, doi: 10.1007/s00190-011-0456-0.

Zebker, H. A., P. A. Rosen, and S. Hensley (1997). Atmospheric effects in interferometric synthetic aperture radar surface deformation and topographic maps, *J. Geophys. Res.* **102,** 7547–7563.

King Abdullah University of Science and Technology (KAUST)
Division of Physical Sciences and Engineering
Thuwal 23955-6900, Saudi Arabia
wenbin.xu@kaust.edu.sa
rishabh.dutta@kaust.edu.sa
sigurjon.jonsson@kaust.edu.sa

Manuscript received 30 September 2014;
Published Online 3 February 2015